Journal of Power Sources 203 (2012) 165–176

Contents lists available at SciVerse ScienceDirect

Journal of Power Sources

journal homepage: www.elsevier.com/locate/jpowsour

Thermal modelling and simulation of the all-vanadium redox flow battery

Ao Tang, Simon Ting, Jie Bao, Maria Skyllas-Kazacos *

School of Chemical Engineering, University of New South Wales, Sydney, NSW 2052, Australia

ARTICLE INFO

Article history:
Received 7 November 2011
Received in revised form
28 November 2011
Accepted 29 November 2011
Available online 8 December 2011

Keywords:
Vanadium redox flow battery
Thermal modelling
Battery temperature
Energy balance

ABSTRACT

Studies have shown that the temperature of the electrolyte solutions in the vanadium redox flow battery (VFB) has a significant impact on the battery performance. In this paper, a thermal model for the VFB has been developed on the basis of the conservation of energy to predict the battery temperature as a function of time under different operating conditions and structure designs. Simulations of battery and electrolyte temperature at both constant and varying environmental temperatures show that the presenting model is able to effectively forecast the fluctuation of the battery temperature in the presence of different charge and discharge currents. As expected, increasing current or reduced flow rate will increase the stack and electrolyte temperature. Thermal properties of the tank material and its surface area can however be adjusted to optimize heat transfer to the atmosphere to reduce overheating. This model can be employed to develop a model-based control system which will manage the electrolyte temperature in the optimal range. Further possible improvements to the model are also discussed.

1. Introduction

With the rapid growth of renewable energy technologies, the renewable energy is expected to be able to gradually substitute the domination of coal-fired energy in electrical energy production, thereby reducing the greenhouse gas emission. In spite of the clean energy, the intermittent nature of most renewable energy restricts the possibility of supplying consistent power throughout the whole day. A large energy storage system is a solution to overcome this drawback. While the conventional secondary batteries face the issues of scale-up and high cost for large-scale applications, the redox flow batteries with the flexibility of determining the storage capacity and output power separately have shown a promising future for large-scale energy storage. Ever since the first redox flow battery concept was proposed in the early 1970s, a variety of redox couples have been investigated and employed in developing high performance redox flow batteries among which the all-vanadium redox flow battery (VFB) initially proposed by Skyllas-Kazacos and co-workers at the University of New South Wales (UNSW) in the mid-1980s has yet reached commercial fruition [1–5].

The evolution of the VRB has experienced two main stages at UNSW in which the Generation 1 All-Vanadium Redox Flow Battery (G1 VFB) was developed in the 1980s and successfully demonstrated by several field trials around the world throughout the rest of the 20th century till nowadays, followed by the emergence of Generation 2 Vanadium/Halide Redox Flow Battery (G2 VFB) with almost doubled specific energy than that of G1 VFB in 2001 and further development undertaken primarily by UNSW and V-Fuel Pty Ltd during the 2000s. Apart from the research carried out at UNSW, several research groups in UK, China and elsewhere have also switched their interests and focuses to vanadium redox flow battery since the new century, covering the topics of development of new low cost membrane, mechanistic study of the vanadium redox couples in different supporting solutions as well as numerical modelling and simulation of the battery performance [6–9].

The electrolyte solutions of the G1 VFB consist of sulfuric acid containing vanadium redox couples with four different states of oxidation V^{2+}/V^{3+}, and V^{4+}/V^{5+} at the negative and positive sides respectively. In general, a G1 VFB electrolyte employing 2 mol L^{-1} vanadium sulfate in 2.5 mol L^{-1} sulfuric acid can undergo daily charging and discharging within a temperature range of 15–35 °C. At temperatures below 5 °C, precipitation of V^{2+}/V^{3+} in the negative electrolyte occurs. Likewise, thermal precipitation of V^{5+} happens at temperatures higher than 40 °C. If not controlled, this precipitation phenomenon could block electrolyte channels and give rise to a deterioration in battery performance. Battery temperature is therefore a very crucial parameter that needs to be considered in the VFB design and controlled for efficient and safe operation. Shah and co-workers [9] developed a non-isothermal model to investigate the temperature in the stack of the VFB under different conditions, but to date, no thermal model has been developed to study the effect of heat transfer on the electrolyte temperature under different operating conditions.

The aim of this paper is to develop a dynamic thermal model based on the conservation of energy and to use the model to simulate the VFB temperature variation as a function of time,

* Corresponding author. Tel.: +61 2 9385 4335; fax: +61 2 9385 5966.
E-mail address: m.kazacos@unsw.edu.au (M. Skyllas-Kazacos).

0378-7753/$ – see front matter © 2011 Elsevier B.V. All rights reserved.
doi:10.1016/j.jpowsour.2011.11.079

surrounding air temperature and battery structure. This model will provide a deep insight into the electrolyte temperature variation and can be useful in the design of VFBs for installations in different regions of the world that have a range of temperature variation. Furthermore, such a dynamic thermal model is useful in the development of an advanced model based battery temperature controller that will ensure efficient operation within operational constrains.

2. Thermal model development

The thermal model development is based on the conservation of energy and several assumptions below are made to simplify the model without loss of generality:

I. No heat transfer occurs in the battery stack and pipes;
II. The heat is only transferred between the electrolyte tanks and the surrounding air;
III. The heat generated in the battery only comes from the resistance in each cell;
IV. The electrolytes are perfectly mixed in both the cells and the tanks;
V. The volume of the electrolyte in both the tanks and the cells remain constant.

Based on the above assumptions and conservation of energy balance, the energy balance equations for the battery stack and the two electrolyte tanks can be respectively described as follows:

In the process of charging

$$C_p\rho V_s\frac{dT_s}{dt} = Q_+C_p\rho(T_+ - T_s) + Q_-C_p\rho(T_- - T_s) + I^2R_c \quad (1)$$

$$C_p\rho V_+\frac{dT_+}{dt} = Q_+C_p\rho(T_s - T_+) + U_+A_+(T_{air} - T_+) \quad (2)$$

$$C_p\rho V_-\frac{dT_-}{dt} = Q_-C_p\rho(T_s - T_-) + U_-A_-(T_{air} - T_-) \quad (3)$$

In the process of discharging, Eq. (1) will be substituted by Eq. (4) in which the overall stack resistance during charging is used, while Eqs. (2) and (3) are still applied.

$$C_p\rho V_s\frac{dT_s}{dt} = Q_+C_p\rho(T_+ - T_s) + Q_-C_p\rho(T_- - T_s) + I^2R_d \quad (4)$$

where

T_s = stack electrolyte temperature, °C
T_+ = temperature of the positive electrolyte in the tank, °C
T_- = temperature of the negative electrolyte in the tank, °C
T_{air} = surrounding air temperature, °C
C_P = specific heat of the electrolyte, J g^{-1} K^{-1}
ρ = electrolyte density, g m^{-3}
V_s = volume of the battery stack, m^3
V_+ = volume of the positive electrolyte in the tank, m^3
V_- = volume of the negative electrolyte in the tank, m^3
Q_b = outlet flow rate of the battery stack, m^3 s^{-1}
Q_+ = outlet flow rate of the positive electrolyte in the tank, m^3 s^{-1}
Q_- = outlet flow rate of the negative electrolyte in the tank, m^3 s^{-1}
U_+ = overall heat transfer coefficient of the tank at positive side, Wm^{-2} K^{-1}
U_- = overall heat transfer coefficient of the tank at negative side, Wm^{-2} K^{-1}
A_+ = surface area of the tank at positive side, m^2
A_- = surface area of the tank at negative side, m^2
I = charging or discharging current, A
R_c = overall stack resistance in charging, Ω
R_d = overall stack resistance in discharging, Ω

Table 1
Parameter values for the simulation.

Parameters	Value
Vanadium concentration, c	1.6 mol L^{-1}
Specific heat of 4.4 M sulfate, C_p	3.2 J g^{-1} K^{-1}
Electrolyte density, ρ	1.354 g cm^{-3}
Number of cell, num	19
Volume of each cell, V_c	30 × 50 × 0.6 cm^3 = 0.9 L
Volume of the stack, V_{stack}	17.1 L
Charging average cell resistivity, R_c	2.9 Ωcm^2
Discharging average cell resistivity, R_d	3.13 Ωcm^2
Electrode area, S	1500 cm^2
Faraday's constant, F	96485 C mol^{-1}
Number of electrons transferred, z	1
Coulombic efficiency, eff	95%
Total electrolyte volume for one half-cell, V_s	10.95 L
Tank radius, r	0.252 m
Tank height, H	1 m
Volume of each tank, V_{tank}	200 L
Polypropylene thickness, θ	0.01 m
Polypropylene conductivity, k	0.16 Wm^{-1} K^{-1}
Convection heat transfer coefficient for the inner cylinder surface, h_{11}	270.1 Wm^{-2} K^{-1}
Convection heat transfer coefficient for the inner top or bottom surface, h_{12}	405.2 Wm^{-2} K^{-1}
Convection heat transfer coefficient for the outer cylinder surface, h_{21}	3.5 Wm^{-2} K^{-1}
Convection heat transfer coefficient for the outer top or bottom surface, h_{22}	5.3 Wm^{-2} K^{-1}

3. Simulation and results

3.1. Parameters

A 2.5 kW/15 kWh VFB system comprising a 19 cell stack was employed in this simulation. All the individual cells were assumed to be exactly the same. The tanks with the shape of cylinder are made of polypropylene with a volume of 200 L typical for a 15 kWh VFB system. Both tanks have the same size and it is assumed the outlet flow rates of both tanks are uniform. All the parameters (see Appendix A) employed in the simulation are summarized in Table 1 and specified in details below.

The electrolyte solution was assumed to contain 2 M vanadium in 4.4 M total sulfate. The density of the electrolyte was taken as 1.354 g cm^{-3} [10] while the specific heat of the electrolyte was assumed to be that of 4.4 M sulfate [11]. The battery stack consists of 19 cells that are made of low-density polyethylene which is a good insulator such that the assumption (i) is reasonable. The electrode and membrane area were set at 1500 cm^2. Additionally, the average cell resistance, including both ohmic and polarization losses, was calculated by implementing a polarization test on a laboratory test battery [12]. As the operating state-of-charge (SOC) was chosen to be from 10% to 90% in the simulation, within which the average cell resistance will not change dramatically, the average cell area resistances of 2.9 Ω cm^2 for charging and 3.13 Ω cm^2 for discharging obtained from the slope of the voltage versus current curves [12] were assumed to be constant.

It was also assumed that the flow rates of all the half-cells are identical with a value of twice the maximum theoretical flow rate calculated on the basis of Faraday's law of electrolysis (Eq. (5)) in which the SOC ranges from 10% to 90%:

$$Q = \frac{2 \times I}{z \times F \times c \times \mathrm{SOC}} \quad (5)$$

where I is the maximum current applied during charge–discharge cycling and SOC is chosen to be the minimum value of 10% in this case. During each charging–discharging cycle, the outlet flow rate of the tank is set to be constant.

The model further assumes that the tanks and battery stack are fully filled with the respective electrolyte solutions and that

no gassing side reactions and ion diffusions occur during operation. The charging and discharging times were thus calculated based on Faraday's law of electrolysis as shown in Eqs. (6) and (7) where V_s is obtained by dividing the total electrolyte in the positive/negative side by the number of cells. In practice, the charging time is much longer than the theoretical value from calculation while the discharging time is shorter due to the self-discharge reactions. Therefore, a factor of 0.95 as the coulombic efficiency of the battery is divided and multiplied in Eqs. (6) and (7) respectively to calculate the charging and discharging times.

$$t_c = \frac{c \times V_s \times z \times F}{(I_c \times \text{eff})} \tag{6}$$

$$t_d = \frac{\text{eff} \times c \times V_s \times z \times F}{I_d} \tag{7}$$

Two cylindrical tanks made of polypropylene were employed in the simulation. It is assumed the cylinder tank is exposed to a free convection environment on its inner and outer isothermal surfaces, which is reasonable in the case that the tanks are stored in a closed space and the flow rate is quite small compared to the volume of the tank. As a result, the heat will be transferred through three thermal resistances including a conduction resistance on polypropylene and two convection resistances mentioned above. The conduction heat transfer can be determined by Fourier's law of heat conduction based on the conductivity of polypropylene, while the convection heat transfer is able to be described by Newton's law of cooling, but this is more difficult to analyze and obtain its coefficients. In this present work, the convective heat transfer coefficients for the air side are chosen to be 3.5 $Wm^{-2}K^{-1}$ (cylinder wall) and 5.3 $Wm^{-2}K^{-1}$ (top and bottom plate) respectively in accordance with the calculation in Appendix B, while 270.1 $Wm^{-2}K^{-1}$ (cylinder wall) and 405.2 $Wm^{-2}K^{-1}$ (top and bottom plate) are obtained for the electrolyte side. The overall heat transfer coefficient for the cylindrical tank, therefore, can be separated into two parts which can be calculated as follows:

The overall heat transfer coefficient for the cylindrical wall of the tank based on the inside area of is

$$U_1 = \frac{1}{(1/h_{11}) + (r/k)\ln(r+\theta/r) + (r/r+\theta)(1/h_{21})} \tag{8}$$

The overall heat transfer coefficient for the top or bottom circular wall of the tank is

$$U_2 = \frac{1}{(1/h_{12}) + (\theta/k) + (1/h_{22})} \tag{9}$$

The inside area of the cylindrical wall A_1 and the area of the top or bottom circular wall A_2 can be calculated by $A_1 = 2 \times \pi \times r \times H$ and $A_2 = \pi \times r^2$. The overall heat transfer across the cylindrical tank, therefore, can be calculated by

$$Q_{\text{heat}} = UA(T_{\text{air}} - T_t) \tag{10}$$

where $UA = U_1A_1 + 2U_2A_2$

3.2. Simulation results

The temperature profiles of the battery were simulated under a number of different charging and discharging currents and air temperatures. The corresponding charging/discharging time was determined by Eqs. (6) and (7). In the present simulations, it was assumed that the battery always starts charging from the hottest time of the day so that the initial temperature of the electrolyte in both the tanks and the stack are equal to the upper level of the air temperature. The investigation of the temperature variation inside the battery can give deep insights into the battery operating status under different conditions that can be considered in the process of battery temperature control system design.

3.2.1. Case 1: constant surrounding air temperature

Starting with a constant surrounding air temperature of 25 °C, the VFB was simulated with different charging and discharging currents. Figs. 1–3 present the simulation results for three sets of charging/discharging currents. As shown in Fig. 1, the electrolyte temperature attains a steady state and oscillates around 26 °C, indicating that no thermal precipitation of V^{5+} would occur under this circumstance [13]. It is also observed that both the tank and stack temperatures increase during discharge while decreasing during the charging process after reaching the steady state. This phenomenon is caused by the smaller cell resistance during the discharge process that results from the faster reaction kinetics of the V(V) reduction process compared with the V(IV) to V(V) oxidation reaction [8]. This leads to different amounts of heat generated by the stack resistances that is the only source producing heat in this case scenario. This is more evident in the simulation of Fig. 2 where a 100 A discharging current was employed, this leading to approximately 400 J s^{-1} difference in heat generation rate between charging and discharging. Despite the increased electrolyte flow rate associated with the use of the larger discharge current, the stack temperature is always higher than the tank temperature as it is assumed that no heat transfer occurs between the stack and the surrounding air. On the other hand, by increasing the charging current to 100 A, both the stack temperature and tank temperature are seen to approach 40 °C where thermal precipitation of V^{5+} could occur if the battery were allowed to stand in the fully charged condition for extended periods for time. It is also noted that the oscillation of the battery temperature during charge–discharge cycling is quite small and even not visible in Fig. 3 as in Fig. 1, since the magnitude of heat generated from the stack resistances does not change dramatically.

3.2.2. Case 2: varying surrounding air temperature

To investigate the battery temperature under different climatic conditions, three sets of air temperature profiles representing a hot climate, a warm climate as well as a cold climate was employed in the simulation. In each case, the effect of charging/discharging current magnitude on the variation of battery temperature was studied. For simplicity, the surrounding air temperature was assumed to have the form of a sine-squared function:

$$T_{\text{air}} = B \cdot \sin^2(\omega t + \varphi) + C \tag{11}$$

where

$(B + C)$ = maximum temperature reached
C = minimum temperature reached
ω = angular frequency, rad s^{-1}
ϕ = phase, rad
t = time, s

3.2.2.1. Moderate summer climate scenario. To simulate a summer temperature profile for a warm climate, a typical daily temperature ranging from 15 °C to 35 °C was firstly employed in the thermal model based on Eq. (11). With both 30 A charging and discharging currents, the electrolyte temperature reduces and finally oscillates around an equilibrium point of 26 °C with the same regular frequency as the air temperature. Because of the relatively small current applied, less heat is produced from the stack resistance which makes a smaller contribution to the variation in battery temperature compared with the surrounding air temperature as shown in Fig. 4. When the discharge current is increased to 100 A, however, an irregular oscillation in the temperature of both the stack and electrolyte tanks is observed in Fig. 5 where the average of the electrolyte temperature is a little higher at around 30 °C. As the electrolyte temperature in both cases is above 5 °C and below 40 °C,

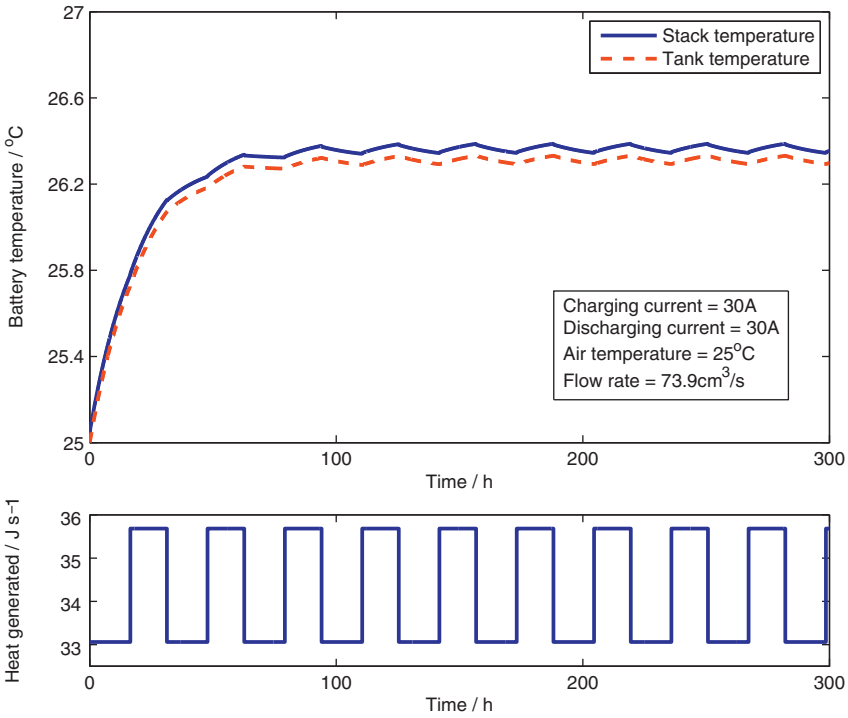

Fig. 1. Battery temperature variation with both 30 A charging and discharging currents at a constant air temperature of 25 °C.

no precipitation would be expected to occur in the VFB system during this type of operation. It is also demonstrated that the battery temperature could generally follow the trend of the air temperature with a large heat transfer capability via the tanks, in spite of being influenced at the charge–discharge switch points, by the heat difference between charge and discharge. By increasing the charging current to 100 A, however, it is seen from Fig. 6 that the increased heat from charging drives the electrolyte temperature up to 42 °C, thereby potentially putting the battery into the thermal precipitation region for the positive electrolyte solution. It is worth noting that the battery temperature also varies sinusoidally in Fig. 6, this being attributed to the small discrepancy in the heat generated between charge and discharge. In general, the smaller difference in the heat produced by the stack resistance during charge and discharge, the closer the tracking of the battery temperature with the surrounding temperature, provided that the electrolyte flow

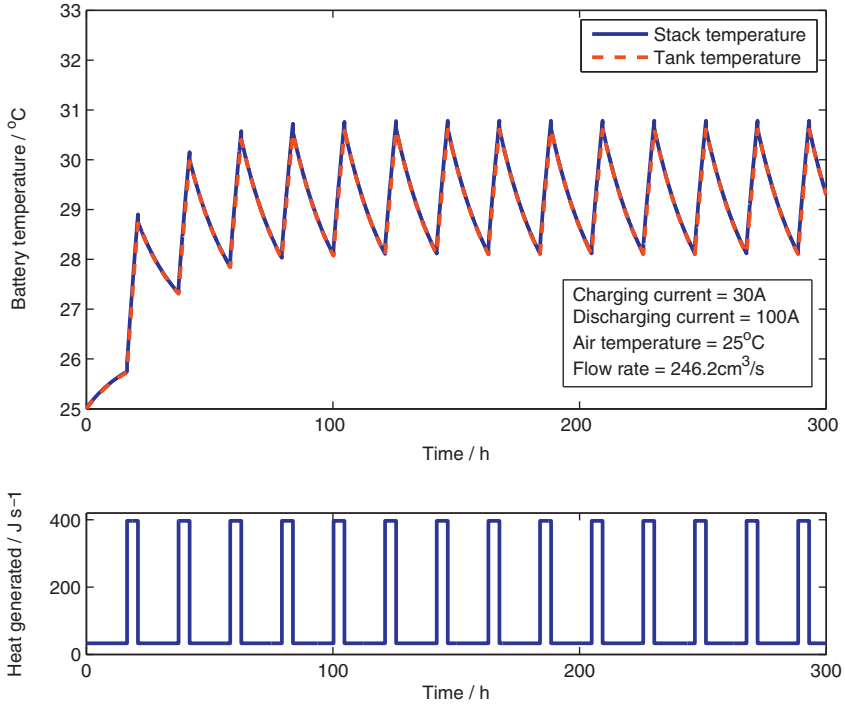

Fig. 2. Battery temperature variation with 30 A charging current and 100 A discharging current at a constant air temperature of 25 °C.

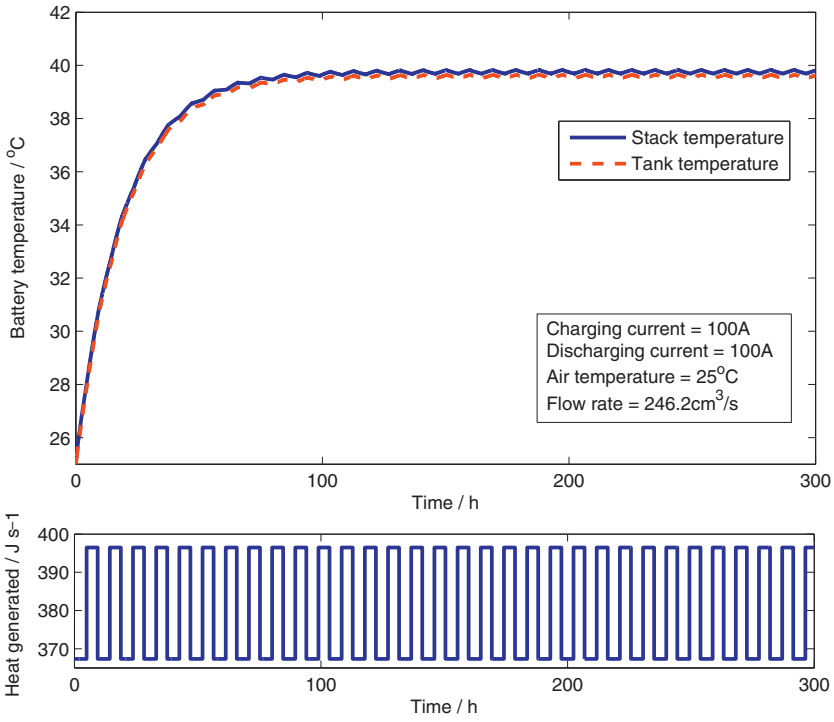

Fig. 3. Battery temperature variation with both 100 A charging and discharging currents at a constant air temperature of 25 °C.

rate is adequate. All the three figures have demonstrated that the surrounding daily air temperature has a significant effect on the battery temperature and this in conjunction with the effect of surrounding air temperature, will interact and determine the final steady state temperature of the battery stack and electrolytes.

3.2.2.2. Moderate winter climate scenario. To investigate the VFB temperature variation during winter in a moderate climate, a daily surrounding air temperature of −5–15 °C was simulated. As expected, Fig. 7 shows that the stack temperatures in both cases have the same trends as in Figs. 4 and 5 while being shifted down

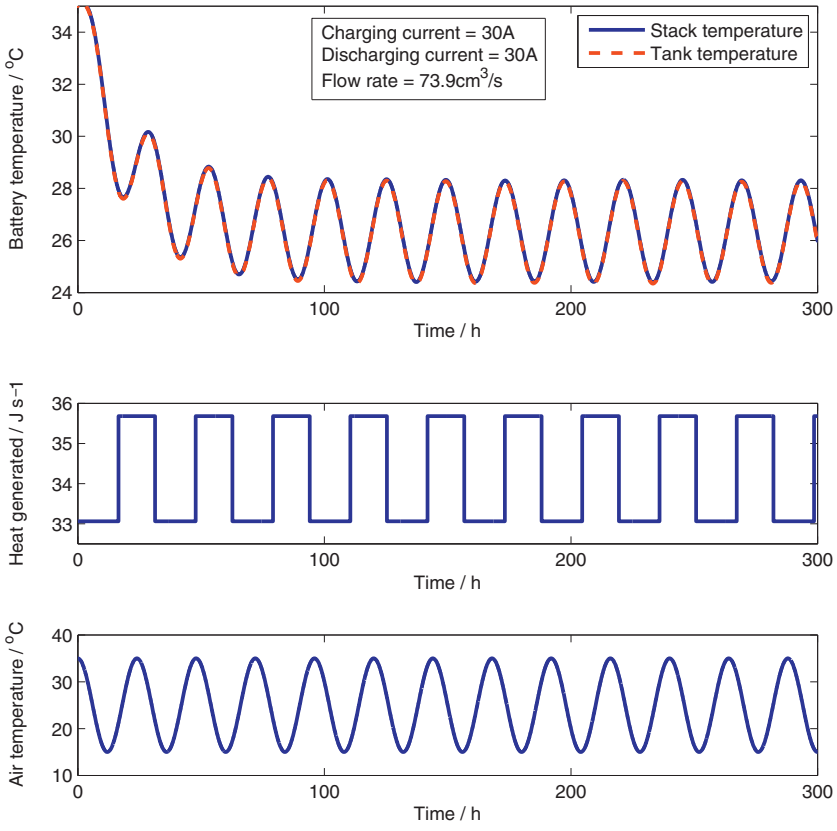

Fig. 4. Battery temperature variation with both 30 A charging and discharging currents under a varying air temperature range from 15 °C to 35 °C.

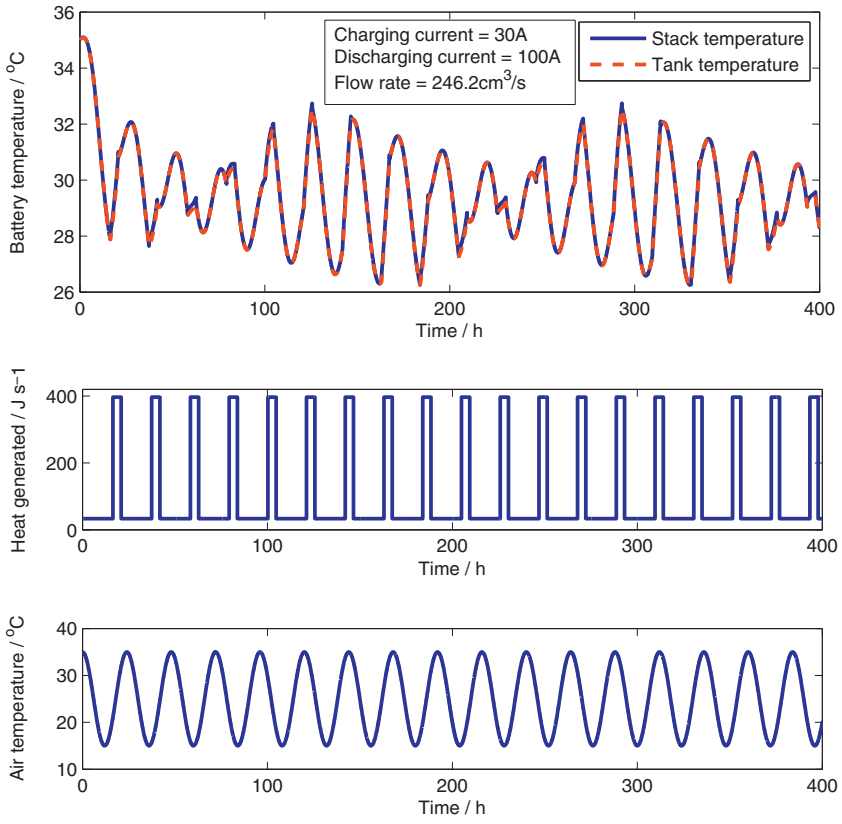

Fig. 5. Battery temperature variation with 30 A charging current and 100 A discharging current under a varying air temperature range from 15 °C to 35 °C.

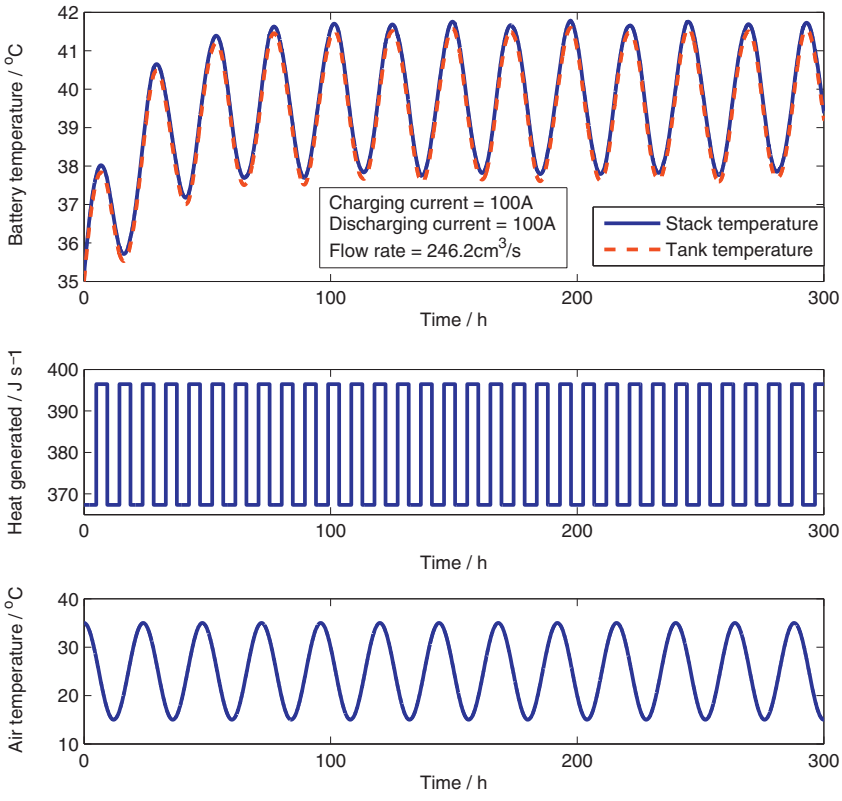

Fig. 6. Battery temperature variation with both 100 A charging and discharging currents under a varying air temperature range from 15 °C to 35 °C.

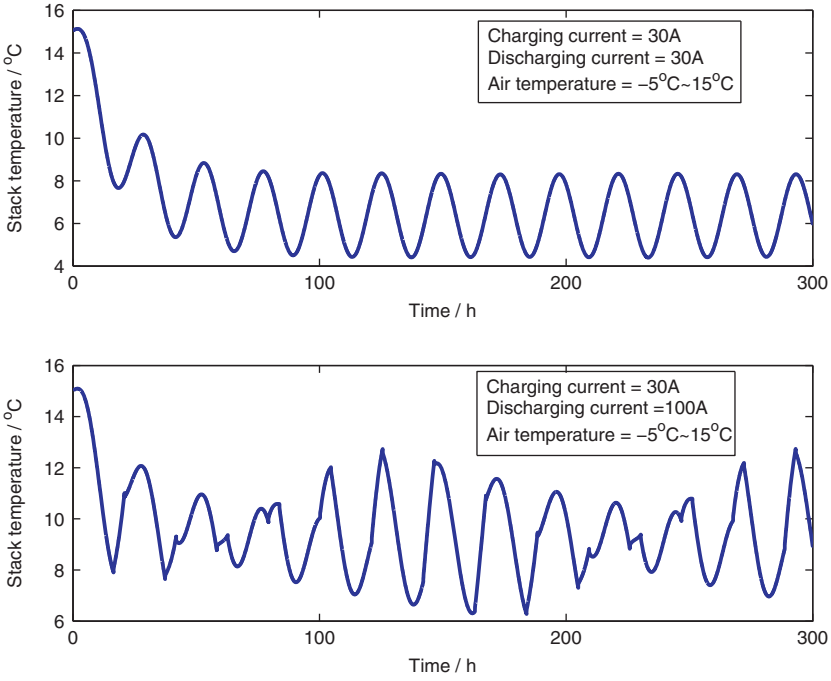

Fig. 7. Stack temperature variation under a varying air temperature range from −5 °C to 15 °C.

by 20 °C overall. Since the both the frequencies of heat and air temperature are not changed, the battery temperature variation will only be shifted up or down depending on the range of air temperature. It can be observed that the stack temperature could drop below 5 °C with 30 A charging and discharging currents, in which case the precipitation of vanadium ions in the negative electrolyte could occur if the electrolyte were allowed to stand at near either 0% or 100% state of charge for extended periods at the low temperatures. On the other hand, increasing the discharge current to 100 A allows the battery temperature to be maintained above 6 °C at all times. The heat plays an important role in the latter scenario, being accumulated to avoid an excessive drop in the electrolyte temperature which could cause precipitation of V^{2+}/V^{3+} in electrolytes containing more than 1.6 M vanadium ions during extended low temperature storage at high or low states of charge when the electrolyte could become supersaturated in either the V^{2+} or V^{3+} ions. It should be mentioned that at intermediate states of charge, both ions would be present at concentrations significantly below their saturation level, so precipitation would not be expected.

3.2.2.3. Cold winter climate scenario. A daily temperature range of −20–0 °C was lastly employed to simulate a typical winter scenario in a cold climate. Without a doubt, the electrolyte temperature is not able to exceed the upper level temperature of 0 °C with charging current of 30 A and discharging current of 100 A or even smaller values as indicated in the above cases. With a current of 100 A for both charging and discharging, it can be anticipated that the electrolyte temperature will be shifted down 35 °C in general and become less than 5 °C. By employing a discharging current of 130 A and a charging current of 100 A, however, Fig. 8 shows that the electrolyte temperature could be increased above 5 °C after approximately 22 h charging–discharging cycling, oscillating around 9 °C in the end such that the influence of precipitation of V^{2+}/V^{3+} could be eliminated. In practise, nevertheless, it might not be desirable to prepare or store the fully charged or fully discharged electrolyte solutions at such a low temperature and a more dilute vanadium electrolyte would be required which will limit the capacity of the VFB. A temperature control system, therefore, is essential under such circumstances by which the electrolyte temperature can be adjusted via heating devices so as to ensure that precipitation is avoided.

3.2.3. Case 3: effect of electrolyte flow rate

The electrolyte solution in the VFB is pumped from the electrolyte reservoirs to the cell stack via the external pipes. The electrolyte can therefore act as a heat exchanger allowing heat to be removed from the cell stack, preventing thermal runaway during high rates of charge and discharge. Electrolyte flow rate thus plays an important role in heat transfer between the stack and the electrolyte reservoirs. In an effort to investigate the effect of flow rate on the battery temperature, the theoretical flow rate calculated on the basis of 100% SOC was initially used in the simulation for the case of charging and discharging the battery with 50 A and 100 A under a constant room temperature of 30 °C.

Referring to Fig. 9, the stack temperature is approximately 2 °C on average higher than the tank temperature throughout the first 200 h charge–discharge cycling due to the slow flow rate that transfers less heat from the stack to the tanks, allowing the heat generated by the stack resistance to be accumulated in the stack. This is followed by immediate tracking of the tank temperature when a step change corresponding to a 5-fold increase in flow rate was introduced at 200 h. As indicated by the battery temperature profile, the magnitude of flow rate will not influence the steady state tank temperature, nor will the frequency of the battery temperature variation be affected in this case due to the excellent capability of heat transfer of the tanks. By increasing the flow rate, however, more heat can indeed be transferred from the stack to the tanks, thereby reducing the stack temperature accordingly as shown after 200 h in Fig. 10.

The flow rate of the battery, therefore, has a crucial role in determining the stack temperature of the VFB and eliminating precipitation in individual cells that could cause blockages. In real-life VFB systems, nevertheless, it is not viable to operate at the theoretical flow rate, since good mass transport is needed to prevent concentration polarization at the electrode surfaces that could lead

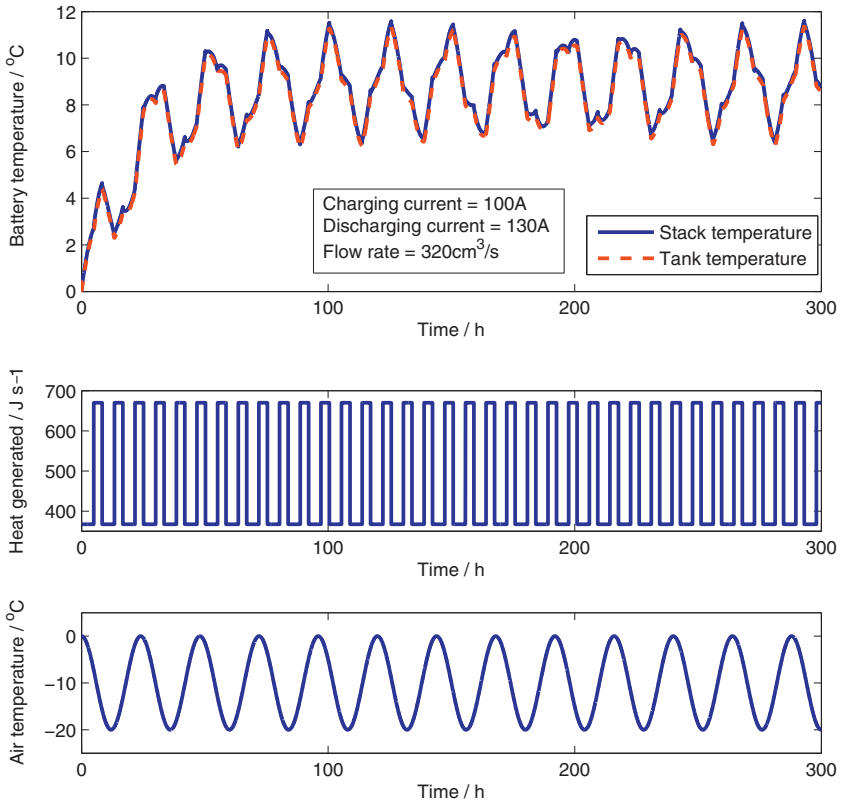

Fig. 8. Battery temperature variation with 100 A charging current and 130 A discharging current under a varying air temperature range from −20 °C to 0 °C.

to electrolysis of water and gassing during charging at high SOC. On the other hand, a faster flow rate can indeed carry more heat from the stack to the storage tanks and release it to the surrounding, thereby acting as a coolant. High flow-rates will however lead to greater pumping energy losses that reduce the overall energy efficiency of the system. Dynamic flow-rate optimization is therefore critical for the efficient operation of the VFB while also allowing stack temperature control, especially when used in combination

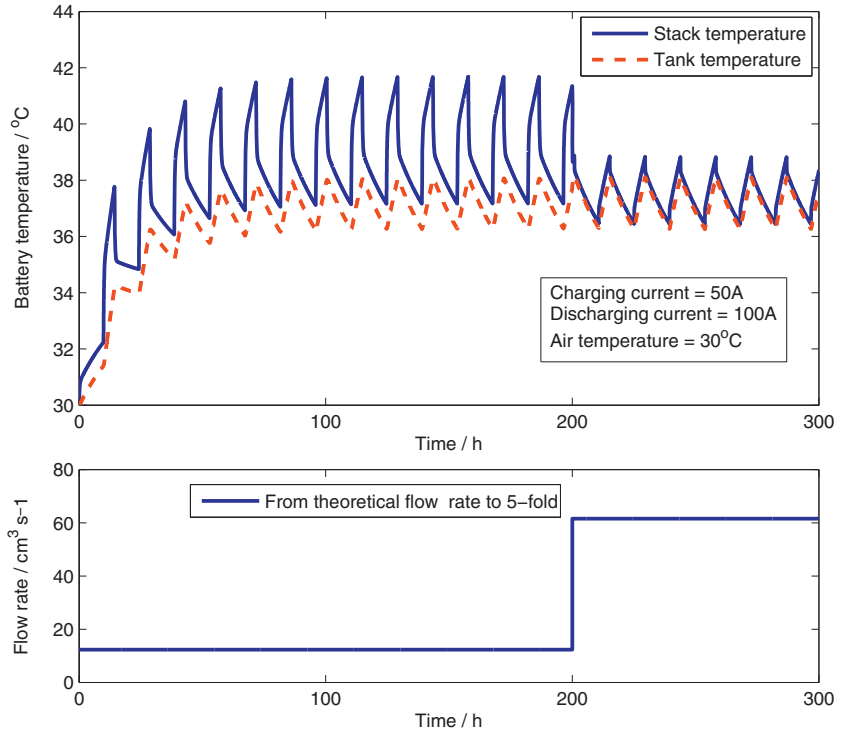

Fig. 9. Battery temperature variation with step change in flow rate under a constant temperature of 30 °C.

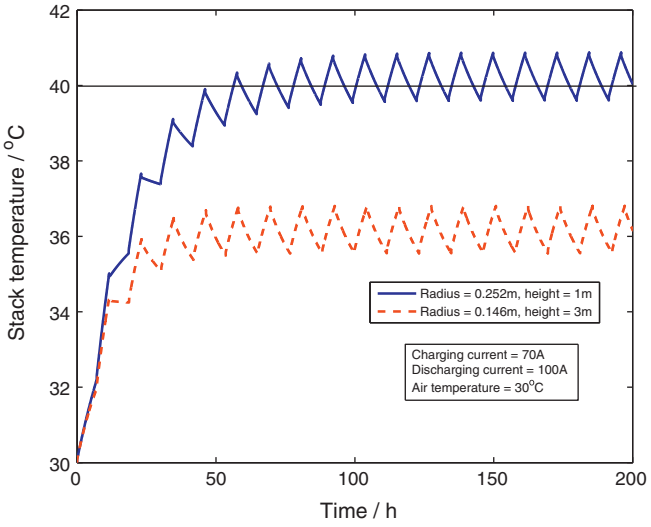

Fig. 10. Stack temperature variation with different dimensions of the tank under a constant air temperature of 30 °C.

with a heat exchanger to enhance the overall heat transfer capability of the system.

3.2.4. Case 4: adjustment of heat transfer capability

In the present model, it has been assumed that heat transfer proceeds only at the surface of the cylindrical electrolyte tanks. A change of heat transfer capability thus can be achieved by changing the electrolyte tank material or geometry. To investigate the effect of heat transfer from the tanks on the electrolyte temperature, the dimensions of the tanks were adjusted in order to increase the total surface area while keeping the tank volume constant. As revealed in Fig. 10, by adjusting the tank radius to 0.146 m and tank height to 3 m the volume of the tank remains constant, whereas the total surface area of the tank has been increased from 1.982 m^2 to 2.886 m^2 providing a better heat transfer capability. It is observed that the stack temperature has dropped from an average of around 41 °C, and now oscillates around 36 °C at a constant surrounding temperature of 30 °C for charging and discharging currents of 70 A and 100 A, respectively. By adjusting the surface area of the tanks, it is therefore possible to enhance heat transfer to the atmosphere, thereby avoiding possible thermal precipitation of V^{5+} in the positive electrolyte solution.

Evidently, a large electrolyte reservoir surface area can offer a fast heat exchange rate between the electrolyte and the surrounding environment, making the surrounding temperature contribute far more to the variation in electrolyte temperature. In hot climate cases, however, a cooling system would be required to cool down the electrolyte temperature regardless of the size of the electrolyte reservoirs. Furthermore, a heating system may need to be implemented if the VFB system is operated in cold temperature conditions, since reducing the size of the tanks to limit the heat transfer may not be feasible due to the pre-set capacity of the VFB which imposes a limitation on the volume of the electrolyte. Apart from the size of the electrolyte tanks, it is also worth noting that other factors such as the material and wall thickness of the tank and the heat exchanged from the pipes (which are not considered in this present study) would also have an impact on the temperature of the VFB system.

3.2.5. Case 5: simulation of a residential power arbitrage scenario

The above simulations have only investigated temperature variation under different conditions without consideration of matching real load profiles to atmospheric temperature variations. Rather than arbitrarily setting the charge–discharge cycling specifications and load profiles therefore, a residential "power arbitrage" scenario was also considered to study the battery temperature in a real-life system. In this simulation, it was assumed that no gassing side reactions and ion diffusion across the membrane occur such that Faraday's law of electrolysis can still be employed to determine the charging and discharging times. Meanwhile, the moderate hot summer climate air temperature profile of Case 2 was used.

For the "power arbitrage" scenario, the 2.5 kW/15 kWh VRB stack of the present model is charged during the off-peak low tariff rate period of 22:00–05:30, followed by a break till 14:00 in the afternoon. From 14:00 to 19:00, the VRB will experience a total 5 h of discharging for the purpose of peak shaving during the peak tariff period, and is subsequently shut down for 3 h ahead of being recharged overnight. During each "off-period" the pump is switched off and it is assumed that no self-discharge reactions occur across the membrane to release heat. The charging and discharging currents are 60 A and 90 A, respectively and are calculated based on an average cell voltage of 1.4 V. All the other specifications are the same as in the hot summer climate case, except for the starting point which is set at 22:00 at night. Correspondingly, the initial electrolyte temperature will be the air temperature at 22:00. The current profile and temperature variation during a single day are shown in Fig. 11, while Fig. 12 illustrates the variation in battery temperature and heat released from resistance losses over 10 days. The simulation results indicate that the electrolyte temperature in both the tanks and the stack oscillate around 30 °C and that the battery operates within a safe temperature range to avoid possible precipitation of vanadium ions in the electrolyte solutions. Thus, this VFB system is able to be operated with a sufficient flow rate and achieve satisfactory performance as a device for residential power arbitrage under the conditions used in this simulation.

4. Discussion

The above simulation results have shown that surrounding air temperature, flow rate, heat transfer surface area and load profile can all impact on battery stack and electrolyte tank temperatures of a VFB. Depending on the total vanadium electrolyte concentration used, extreme high or low temperatures may lead to precipitation of vanadium ions in the electrolyte solutions which may in turn influence battery performance and life cycle. Precipitation may be prevented by reducing the total vanadium ion concentration to suit the particular climatic conditions or by including a heating or cooling system to control temperature. The former approach will reduce the energy density of the system, while the latter will reduce energy efficiency. The use of a thermal model to predict the expected battery temperature ranges for different climatic conditions and load profiles is therefore a valuable tool that can be used to optimize battery design for optimal heat transfer and temperature control. However, it is worth investigating the factors that limit the accuracy of the model prediction and further enhancing the performance of the VFB.

In spite of being governed by Newton's law of cooling, heat transfer by convection is difficult to analyze owing to the complex uncertain mechanism that varies from situation to situation. As such, the convection heat transfer coefficient in Newton's law of cooling depends upon a number of factors such as fluid velocity and viscosity, surface roughness, type of media as well as heat flux. In practice, therefore, the analysis of heat transfer by convection is usually undertaken empirically. In the present work, a few assumptions have been made in order to calculate the convection heat transfer coefficients. The values of convection heat transfer coefficients calculated, nevertheless, are generally reasonable to be employed in the simulation for the purpose of investigating the

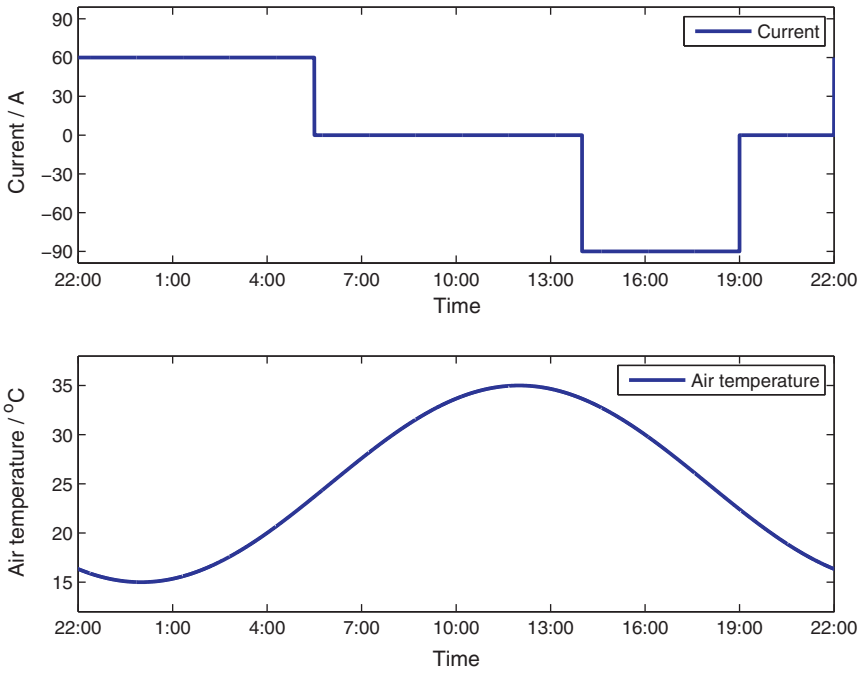

Fig. 11. The current and air temperature profiles in 24 h.

battery temperature variation. To obtain a more accurate value of convection heat transfer coefficient, experiments could be undertaken on the basis of a practical battery design and specification.

In the present model, the self-discharge reactions associated with the diffusion of vanadium ions across the membrane have been ignored. Self-discharge reactions between the different vanadium ions will release heat, the rate of which will depend on the membrane properties. For fast charge–discharge rates, the amount of heat generated by the self-discharge reactions will be negligible compared to that of generated from the stack resistance losses so the model predictions are likely to be correct. In the case of slow charge–discharge cycling or during periodic idle periods, however, the heat produced by self-discharge reactions will make a significant contribution to the total heat generation and should be considered in the model to improve the accuracy of the prediction.

With respect to the flow rate in practice, it is driven by the pumping energy that constitutes a parasitic energy loss for the system. High flow rates (above the theoretical flow rate) will

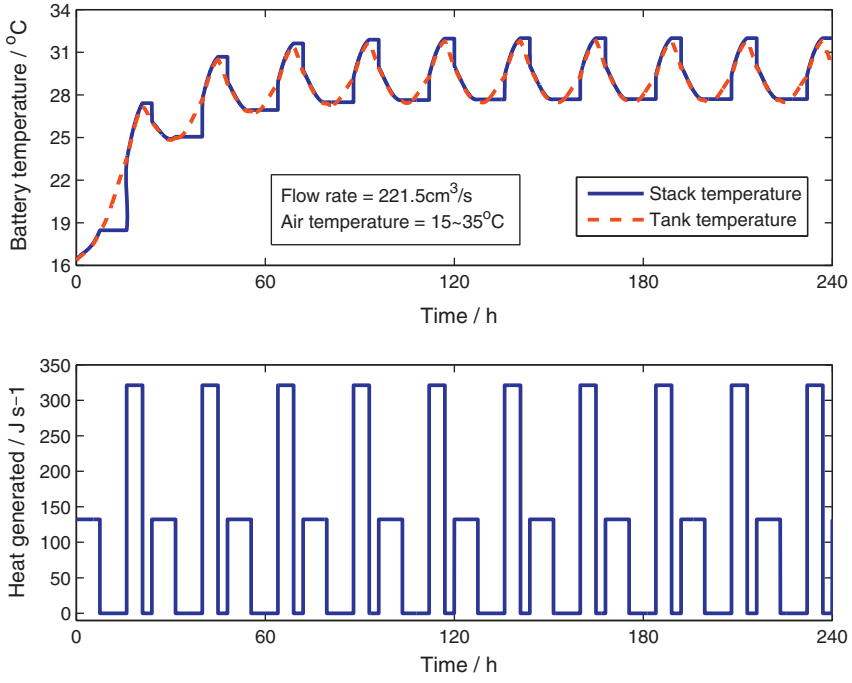

Fig. 12. Battery temperature variation of a 5 kW/15 kWh VRB stack for residential power arbitrage scenario.

ensure good mass transport and reduce concentration overvoltage losses. The theoretical flow rate varies with current and state-of-charge. To minimize pumping energy losses, it is desirable to adjust the flow rate dynamically, just above the theoretical flow rate, in accordance with the state-of-charge and current. In this case, the effect of the flow rate on the stack temperature can be significant. As shown in the case study presented in Section 3.2.3, the stack temperature can exceed the permissible range when a low flow rate is used. The thermal model in this paper can be used in conjunction with the theoretical flow rate model to develop an energy efficient dynamic flow and temperature control system.

Additionally, the pipe and stack will also transfers heat to the surrounding environment and impact on electrolyte and battery temperature. For consecutive charging–discharging cycling, heat transfer from the pumps could also accumulate in the electrolyte to some extent. It is thus desirable to incorporate all these factors into the model for more accurate battery temperature prediction. Last but not least, further investigation and simulation with regard to battery temperature should be linked to specific VFB demonstrations or applications in which the role or the function of the VRB system could be entirely different. Examples include peak shaving, load leveling, electrical power backup, etc. In the meanwhile, a more specific VRB design is preferable to be employed such that all the parameters in the simulation can be calculated and determined more accurately which, in turn, will offer a superior performance prediction that can help in decision making for electrolyte temperature monitoring and control.

All of these factors will be taken into account in the future to develop a more detailed thermal model for the VFB system which can be employed to simulate the battery temperature variation under a variety of different operating conditions. This will provide more insights into the design of the battery system for different applications applied to regions of the world with various climates. For instance, in low temperature areas, battery designs could employ better insulation materials for the tanks and pipes such that the temperature of the battery will not drop too low. Meanwhile, such a detailed thermal model will also assist in developing advanced model-based control strategies for a model predictive temperature control system which would be quite suitable for battery control due to its ability to deal with constrains of the input and output variables.

5. Conclusion

A thermal model for the vanadium redox flow battery system has been developed and presented in this paper. Based on the conservation of energy and several assumptions to simplify the model, three energy balance equations have been set up for the battery stack and the two electrolyte storage tanks. By using a stack containing 19 cells and two cylindrical electrolyte tanks, simulations have been performed under different air temperatures and operating conditions for a 2.5 kW/15 kWh VRB system as a typical case study. The results have shown that the electrolyte temperatures in both the tanks and stack are influenced by multiple effects of flow rate, surrounding temperature and heat generated by cell resistance losses. Hence, this thermal model can be employed to help investigate the possible variation of the battery temperature in the stack at the specific location of the installation and make decisions on the design of the VFB structure and materials. Furthermore, this model will also facilitate the development of an efficient temperature control system to ensure the battery temperature can be managed within the required operational range.

Appendix A. Nomenclature

A	surface area of the tank (m^2)
A_1	inside area of the cylindrical wall (m^2)
A_2	area of the top or bottom circular wall (m^2)
B	amplitude of the air temperature
C	the minimum of the air temperature (°C)
c	Vanadium concentration ($mol\,L^{-1}$)
C_p	specific heat of 4.4 M sulfate ($Jg^{-1}\,K^{-1}$)
eff	Coulombic efficiency
F	Faraday's constant ($C\,mol^{-1}$)
H	tank height (m)
h_{11}	convection heat transfer coefficient for the inner cylinder surface ($Wm^{-2}\,K^{-1}$)
h_{12}	convection heat transfer coefficient for the inner top or bottom surface ($Wm^{-2}\,K^{-1}$)
h_{21}	convection heat transfer coefficient for the outer cylinder surface ($Wm^{-2}\,K^{-1}$)
h_{22}	convection heat transfer coefficient for the outer top or bottom surface ($Wm^{-2}\,K^{-1}$)
I	current (A)
k	thermal conductivity of polypropylene ($Wm^{-1}\,K^{-1}$)
num	number of cell
Q	outlet flow rate ($m^3\,s^{-1}$)
Q_{heat}	Heat transfer rate ($J\,s^{-1}$)
R	overall stack resistance (Ω)
R_{c0}	charging average cell resistivity (Ω)
R_{d0}	discharge average cell resistivity (Ω)
r	tank radius (m)
S	electrode area (cm^2)
SOC	state of charge
T	temperature (°C)
t	time (s)
U	overall heat transfer coefficient ($Wm^{-2}\,K^{-1}$)
U_1	overall heat transfer coefficient for the cylindrical wall of the tank ($Wm^{-2}\,K^{-1}$)
U_2	overall heat transfer coefficient for the top circular wall of the tank ($Wm^{-2}\,K^{-1}$)
z	electrons involved in the reaction
Greek symbols	
ρ	electrolyte density ($g\,cm^{-3}$)
θ	tank thickness (m)
ω	angular frequency ($rad\,s^{-1}$)
ϕ	phase (rad)
Subscript	
air	surrounding air
c	charging
d	discharging
s	stack
t	tank
+	positive side
−	negative side

Appendix B.

The free convection heat transfer mode is assumed for both inner and outer layers of the tanks. The average free convection heat transfer coefficients can be represented in the following form for a variety of circumstances:

$$\mathrm{Nu}_f = C(\mathrm{Ra})^m$$

where Nu is the Nusselt number, Ra is the Rayleigh number, C and m are the constant values specified for different cases empirically, f indicates the film temperature defined as the arithmetic mean between the wall and free-stream temperature.

The Nusselt number is the ratio of convective to conductive heat transfer across the boundary which is dimensionless

$$\mathrm{Nu} = \frac{hx}{k_f}$$

where

h = convective heat transfer coefficient
x = characteristic length

k_f = thermal conductivity of the fluid

The Rayleigh number is the product of the Grashof and Prandtl number:

$$\mathrm{Ra} = \mathrm{Gr}Pr$$

The Prandtl number is also a dimensionless number representing the ratio of kinematic viscosity to thermal diffusivity

$$Pr = \frac{C_p \mu}{k}$$

where

C_p = specific heat
μ = dynamic viscosity
k = thermal conductivity

The Grashof number is a dimensionless number usually used in fluid dynamics and heat transfer

$$\mathrm{Gr} = \frac{g\beta \Delta T x^3}{\nu^2}$$

where

g = acceleration due to gravity
β = volumetric thermal expansion coefficient (approximately equal to $1/T$)
ΔT = temperature difference between the wall and free-steam
$\nu = u/\rho$ = kinematic viscosity
x = characteristic length

Assuming the film temperature is 27 °C (300 K), the properties of air at atmosphere pressure are [14]

$$\beta = \frac{1}{300} \quad \nu = 15.69 \times 10^6 \mathrm{m^2 s^{-1}}$$

$$k = 0.02624\,\mathrm{W m^{-1} K^{-1}} \quad Pr = 0.708$$

Assuming the temperature difference between the wall and the stream is 26 °C, the Gr Pr product can be calculated as

For the vertical cylinder wall

$$\mathrm{Ra} = \mathrm{Gr}Pr = \frac{(9.8)(0.00333)(26)(1^3)}{(15.69 \times 10^{-6})^2}(0.708) = 2.4402 \times 10^9$$

For the horizontal top and bottom wall

$$\mathrm{Ra} = \mathrm{Gr}Pr = \frac{(9.8)(0.00333)(26)(0.1262^3)}{(15.69 \times 10^{-6})^2}(0.708) = 4.9047 \times 10^6$$

where $x = AP^{-1} = 0.1262$, A is the area and P is the perimeter of the surface.

Therefore, the values of C and m can be obtained from the existing data table for isothermal surfaces and the convection heat transfer coefficient can be calculated as

For the vertical cylinder wall

$\mathrm{Nu} = (0.1)(2.1102 \times 10^9)^{1/3} = 134.63$

$h = \mathrm{Nu}\frac{k}{x} = 3.53\ \mathrm{W m^{-2} K^{-1}}$

For the horizontal top and bottom plates

$$\mathrm{Nu} = (0.54)(4.9047 \times 10^6)^{1/4} = 25.4124$$

$h = \mathrm{Nu}\frac{k}{x} = 5.28\ \mathrm{W m^{-2} K^{-1}}$

In an effort to calculate convection heat transfer coefficient for the inner electrolyte layer, the thermal properties of sulfuric acid is employed rather than vanadium sulfate. Assuming the film temperature is 25 °C, the thermal properties of sulfuric acid are

$C_p = 3.67 \times 10^3\ \mathrm{J kg^{-1} K^{-1}}$ (15.63% H_2SO_4 at 20 °C) [11]

$P = 1100\ \mathrm{kg m^{-3}}$ (estimated) [15]

$\mu = 2.42 \times 10^{-2}\ \mathrm{kg m^{-1} s^{-1}}$ [16]

$k = 0.33\ \mathrm{W m^{-1} °C^{-1}}$ [17]

Assuming the temperature different between the wall and the stream is 30 °C, the convection heat transfer coefficients can be calculated in the same way as derived above

For the vertical cylinder wall

$\mathrm{Ra} = \mathrm{Gr\,Pr} = 5.483 \times 10^{11}$

$\mathrm{Nu} = (0.1)(5.483 \times 10^{11})^{1/3} = 818.4866$

$h = \mathrm{Nu}\frac{k}{x} = 270.1\ \mathrm{W m^{-2} K^{-1}}$

For the horizontal top and bottom plates

$\mathrm{Ra} = \mathrm{Gr\,Pr} = 1.102 \times 10^9$

$\mathrm{Nu} = 0.15(1.102 \times 10^9)^{1/3} = 154.94$

$h = \mathrm{Nu}\frac{k}{x} = 405.15\ \mathrm{W m^{-2} K^{-1}}$

where $x = AP^{-1} = 0.1262$, A is the area and P is the perimeter of the surface.

References

[1] E. Sum, M. Rychcik, M. Skyllas-kazacos, J. Power Sources 16 (1985) 85–95.
[2] M. Skyllas-kazacos, M. Rychick, R. Robins, All-vanadium redox battery, United States Patent, No. 4,786,567 (1988).
[3] M. Skyllas-Kazacos, M. Rychcik, R.G. Robins, A.G. Fane, M.A. Green, J. Electrochem. Soc. 133 (1986) 1057–1058.
[4] M. Skyllas-Kazacos, Encyclopedia of Electrochemical Power Sources, Elsvier, Amsterdam, 2009, pp. 444–453.
[5] M. Skyllas-Kazacos, G. Kazacos, G. Poon, H. Verseema, Int. J. Energy. Res. 34 (2010) 182–189.
[6] P. Zhao, H. Zhang, H. Zhou, J. Chen, S. Gao, B. Yi, J. Power Sources 162 (2006) 1416–1420.
[7] Q. Luo, H. Zhang, J. Chen, P. Qian, Y. Zhai, J. Membr. Sci. 311 (2008) 98–103.
[8] M. Gattrell, J. Park, B. MacDougall, J. Apte, S. McCarthy, C.W. Wu, J. Electrochem. Soc. 151 (2004) A123–A130.
[9] H. Al-Fetlawi, A.A. Shah, F.C. Walsh, Electrochim. Acta 55 (2009) 78–89.
[10] A. Mousa, Chemical and electrochemical studies of V(III) and V(II) solutions in sulfuric acid solution for vanadium battery applications, Ph.D. Thesis, UNSW, 2003.
[11] R.H. Perry, G. Green, Perry's Chemical Engineers' Handbook, sixth ed., McGraw-Hill International Editions, 1984.
[12] M. Skyllas-Kazacos, C. Menictas, Proceeding of International Telecommunications Energy Conference, 1997, pp. 463–471.
[13] F. Rahman, M. Skyllas-Kazacos, J. Power Sources 189 (2009) 1212–1219.
[14] J.P. Holman, Heat Transfer, tenth Ed., McGraw-Hill Higher Education, 2010.
[15] http://en.wikipedia.org/wiki/Sulfuric_acid, last accessed: Oct. 2011.
[16] http://en.wikipedia.org/wiki/Viscosity, last accessed: Oct. 2011.
[17] T.R. Bump, W.L. Sibbitt, Ind. Eng. Chem. 47 (1955) 1665–1670.